Tunable damping, saturation magnetization, and exchange stiffness of half-Heusler NiMnSb thin films

P. Dürrenfeld,[1,*] F. Gerhard,[2] J. Chico,[3] R. K. Dumas,[1,4] M. Ranjbar,[1] A. Bergman,[3] L. Bergqvist,[5,6] A. Delin,[3,5,6] C. Gould,[2] L. W. Molenkamp,[2] and J. Åkerman[1,4,5]

[1]*Department of Physics, University of Gothenburg, 412 96 Gothenburg, Sweden*

[2]*Physikalisches Institut (EP3), Universität Würzburg, 97074 Würzburg, Germany*

[3]*Department of Physics and Astronomy, Uppsala University, Box 520, 752 20 Uppsala, Sweden*

[4]*NanOsc AB, 164 40 Kista, Sweden*

[5]*Materials and Nano Physics, School of ICT, KTH Royal Institute of Technology, Electrum 229, 164 40 Kista, Sweden*

[6]*Swedish e-Science Research Centre (SeRC), 100 44 Stockholm, Sweden*

(Received 28 September 2015; published 16 December 2015)

The half-metallic half-Heusler alloy NiMnSb is a promising candidate for applications in spintronic devices due to its low magnetic damping and its rich anisotropies. Here we use ferromagnetic resonance (FMR) measurements and calculations from first principles to investigate how the composition of the epitaxially grown NiMnSb influences the magnetodynamic properties of saturation magnetization M_S, Gilbert damping α, and exchange stiffness A. M_S and A are shown to have a maximum for stoichiometric composition, while the Gilbert damping is minimum. We find excellent quantitative agreement between theory and experiment for M_S and α. The calculated A shows the same trend as the experimental data but has a larger magnitude. In addition to the unique in-plane anisotropy of the material, these tunabilities of the magnetodynamic properties can be taken advantage of when employing NiMnSb films in magnonic devices.

DOI: 10.1103/PhysRevB.92.214424 PACS number(s): 75.70.−i, 76.50.+g, 71.15.Mb

I. INTRODUCTION

Interest in the use of half-metallic Heusler and half-Heusler alloys in spintronic and magnonic devices is steadily increasing [1–3], as these materials typically exhibit both a very high spin polarization [4–8] and very low spin-wave damping [9–12]. One such material is the epitaxially grown half-Heusler alloy NiMnSb [13,14], which not only has one of the lowest known spin-wave damping values of any magnetic metal, but also exhibits an interesting and tunable combination of twofold in-plane anisotropy [15] and moderate out-of-plane anisotropy [10], all potentially interesting properties for use in both nanocontact-based spin-torque oscillators [16–22] and spin Hall nano-oscillators [23–27]. To successfully employ NiMnSb in such devices, it is crucial to understand, control, and tailor both its magnetostatic and magnetodynamic properties, such as its Gilbert damping (α), saturation magnetization (M_S), and exchange stiffness (A).

Here we investigate these properties in $Ni_{1-x}Mn_{1+x}Sb$ films using ferromagnetic resonance (FMR) measurements and calculations from first principles for compositions of $-0.1 \leqslant x \leqslant 0.4$. M_S and A are shown experimentally to have a maximum for stoichiometric composition, while the Gilbert damping is minimum; this is in excellent quantitative agreement with calculations of and experiment on M_S and α. The calculated A shows the same trend as the experimental data but with an overall larger magnitude. We also demonstrate that the exchange stiffness can be easily tuned over a wide range in NiMnSb through Mn doping, and that the ultralow damping persists over a wide range of exchange stiffnesses. This unique behavior makes NiMnSb ideal for tailored spintronic and magnonic devices. Finally, by comparing the experimental results with first-principles calculations, we also conclude that the excess Mn mainly occupies Ni sites and that interstitial doping plays only a minor role.

II. METHODS

A. Thin-film growth

The NiMnSb films were grown by molecular beam epitaxy onto InP(001) substrates after deposition of a 200-nm-thick (In,Ga)As buffer layer [15]. The films were subsequently covered *in situ* by a 10-nm-thick magnetron-sputtered metal cap to avoid oxidation and surface relaxation [28]. The Mn content was controlled during growth via the temperature, and hence the flux, of the Mn effusion cell. Six different samples (see Table I) were grown with increasing Mn concentration, sample 1 having the lowest and sample 6 the highest concentration of Mn. High-resolution x-ray diffraction (HRXRD) measurements give information on the structural properties of these samples, confirming the extremely high crystalline quality of all samples with different Mn concentration, even in the far-from-stoichiometric cases (samples 1 and 6) [15]. The vertical lattice constant is found to increase with increasing Mn concentration and, assuming a linear increase [29], we estimate the difference in Mn concentration across the whole set of samples to be about 40 at.%. We will thus represent the Mn concentration in the following experimental results by the measured vertical lattice constant. Stoichiometric NiMnSb exhibits vertical lattice constants in the range of 5.96–6.00 Å, leading to the expectation of stoichiometric NiMnSb in samples 2 and 3 [15]. Finally, the layer thicknesses are also determined from the HRXRD measurements, giving an accuracy of ±1 nm.

*philipp.durrenfeld@physics.gu.se

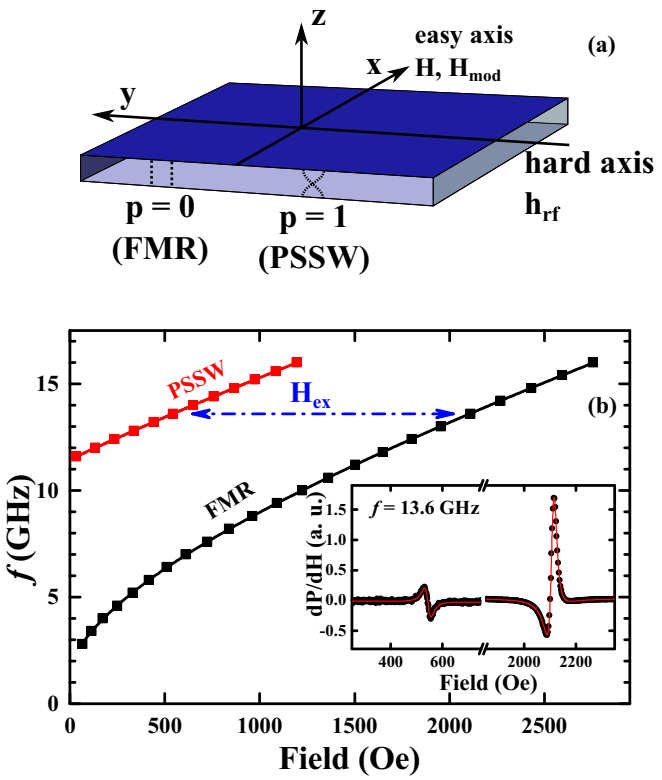

FIG. 1. (Color online) (a) Schematic diagram of the FMR measurement showing field directions. In our setup, the FMR mode and the first PSSW mode are excited. (b) Frequency vs resonance fields of the PSSW (red) and uniform FMR (black) mode for sample 2. The solid lines are fits to the Kittel equation, and both modes are offset horizontally by H_{ex}. Inset: Resonance curves for $f = 13.6$ GHz. The first PSSW mode on the left and the FMR mode on the right were fit with Eq. (1).

B. Ferromagnetic resonance

Broadband field-swept FMR spectroscopy was performed using a NanOsc Instruments PhaseFMR system with a coplanar waveguide for microwave field excitation. Microwave fields h_{rf} with frequencies of up to 16 GHz were applied in the film plane, perpendicularly oriented to an in-plane dc magnetic field H. The derivative of the FMR absorption signal was measured using a lock-in technique, in which an additional low-frequency modulation field $H_{\mathrm{mod}} < 1$ Oe was applied using a pair of Helmholtz coils parallel to the dc magnetic field. The field directions are shown schematically in Fig. 1(a), and a typical spectrum measured at 13.6 GHz is given in the inset of Fig. 1(b). In addition to the zero-wave-vector uniform FMR mode seen at about $H = 2.1$ kOe, an additional weaker resonance is observed at a much lower field of about 500 Oe and is identified as the first exchange-dominated perpendicular standing spin-wave (PSSW) mode. The PSSW mode has a nonzero wave vector pointing perpendicular to the thin-film plane and a thickness-dependent spin-wave amplitude and phase [30,31]. This can be efficiently excited in the coplanar waveguide geometry due to the nonuniform strength of the microwave field across the film thickness [32].

The field dependence of the absorption spectra [inset of Fig. 1(b)] can be fit well (red line) by the sum of a symmetric and an antisymmetric Lorentzian derivative [33,34]:

$$\frac{dP}{dH}(H) = \frac{-8C_1\Delta H(H-H_0)}{[\Delta H^2 + 4(H-H_0)^2]^2} + \frac{2C_2(\Delta H^2 - 4(H-H_0)^2)}{[\Delta H^2 + 4(H-H_0)^2]^2}, \quad (1)$$

where H_0 is the resonance field, ΔH the FWHM, and C_1 and C_2 fitted parameters representing the amplitude of the symmetric and antisymmetric Lorentzian derivatives, respectively. Both the FMR and the PSSW peaks can be fitted independently, as they are well separated by the exchange field $\mu_0 H_{ex} \propto (\pi/d)^2$, where d is the thickness of the layer. For our chosen sample thicknesses, the differences in resonance fields are always much larger than the resonance linewidths.

The field dependence of both resonances is shown in Fig. 1(b) and can now be used to extract information about the magnetodynamic properties and anisotropies of the films. The curves are fits to the Kittel equation, including internal fields from the anisotropy and the exchange field for the PSSW excitation [15,35],

$$f = \frac{\gamma\mu_0}{2\pi}\left[\left(H_0 + \frac{2K_U}{M_S} - \frac{2K_1}{M_S} + H_{ex}\right) \times \left(H_0 + \frac{2K_U}{M_S} + \frac{K_1}{M_S} + H_{ex} + M_{\mathrm{eff}}\right)\right]^{1/2}, \quad (2)$$

where H_0 is the resonance field, $\gamma/2\pi$ the gyromagnetic ratio, and μ_0 the permeability of free space. M_{eff} is the effective magnetization, which has a value close to the saturation magnetization M_S. $2K_U/M_S$ and $2K_1/M_S$ stand for the internal anisotropy fields coming from the uniaxial (K_U) and biaxial (K_1) anisotropy energy densities in the half-Heusler material. The effective magnetic field also includes an exchange field $\mu_0 H_{ex} = (2A/M_S)(p\pi/d)^2$, which is related to the exchange stiffness A, the film thickness d, and the integer order of the PSSW mode p, where $p = 0$ denotes the uniform FMR excitation and $p = 1$ the first PSSW mode. This mode numbering reflects boundary conditions with no surface pinning of the spins, which is expected for the in-plane measurement geometry [36].

We stress that the expression for the anisotropy contribution in Eq. (2) is only valid for the case in which the magnetization direction is parallel to the uniaxial easy axis and also parallel to the applied field. A full angular-dependent formulation of the FMR condition is described in Ref. [15]. To fulfill the condition of parallel alignment for all resonances, we perform the FMR measurements with the dc magnetic field being applied along the dominant uniaxial easy axis of each film, which changes from the [110] crystallographic direction to the [1$\bar{1}$0] direction with increasing Mn concentration (see Table I).

The values of the biaxial anisotropy $\frac{2K_1}{M_S}$ have been determined in a previous study by fixed-frequency, in-plane, angular-dependent FMR measurements [15] and were thus taken as constant values in the fitting process for Eq. (2); a simultaneous fit of both contributions can yield arbitrary combinations of anisotropy fields due to their great interdependence. The values for the uniaxial anisotropy $\frac{2K_U}{M_S}$ obtained from the

TABLE I. Overview of NiMnSb films investigated in this study.

Sample	Vertical lattice constant (Å)	Thickness (nm)	Uniaxial easy axis	$\frac{2K_1}{M_S}$ (Oe)
1	5.94	38	[110]	170
2	5.97	38	[110]	8.4
3	5.99	40	[110]	0
4	6.02	45	[1$\bar{1}$0]	9.0
5	6.06	45	[1$\bar{1}$0]	14.2
6	6.09	38	[1$\bar{1}$0]	25.5

frequency-dependent fitting are in very good agreement with the previously obtained values in Ref. [15]. The gyromagnetic ratio was measured to be $\gamma/2\pi = (28.59 \pm 0.20)$ GHz/T for all investigated samples and was therefore fixed for all samples to allow better comparison of the effective magnetization values.

The Gilbert damping α of the films is obtained by fitting the FMR linewidths ΔH with the linear dependence [37]

$$\mu_0 \Delta H = \mu_0 \Delta H_0 + \frac{4\pi\alpha}{\gamma} f, \tag{3}$$

where ΔH_0 is the inhomogeneous linewidth broadening of the film. The parallel alignment between magnetization and external magnetic field ensures that the linewidth is determined by the Gilbert damping process only [38].

C. Calculations from first principles

The electronic and magnetic properties of the NiMnSb half-Heusler system were studied via first-principles calculations. The material was assumed to be ordered in a face-centered tetragonal structure with an in-plane lattice parameter $a_{\text{lat}}^{\parallel} = 5.88$ Å, close to the lattice constant of the InP substrate, and an out-of-plane lattice constant of $a_{\text{lat}}^{\perp} = 5.99$ Å, matching the value for the stoichiometric composition. Fixed values for the lattice parameters were chosen since an exact relation between the off-stoichiometric composition and the experimentally measured vertical lattice constants cannot be established. Moreover, calculations with a varying vertical lattice parameter for a constant composition showed only a negligible effect on M_S, A, and α. The calculations were performed using the multiple scattering Korringa-Kohn-Rostoker (KKR) Green's function formalism as implemented in the SPRKKR package [39]. Relativistic effects were fully taken into account by solving the Dirac equation for the electronic states, the shape of the potential was considered via the atomic sphere approximation (ASA), and the local spin density approximation (LSDA) was used for the exchange correlation potential. The coherent potential approximation (CPA) [40,41] was employed to treat the chemical disorder of the system.

The Gilbert damping α of the material was calculated using linear response theory [42], including the temperature effects from interatomic displacements and spin fluctuations [43,44].

The exchange interactions J_{ij} between the atomic magnetic moments were calculated using the magnetic force theorem, as considered in the Liechtenstein-Katsnelson-Antropov-Gubanov (LKAG) formalism [45,46]. The interactions were calculated for up to 4.5 times the lattice constant in order to take into account any long-range interactions. Given the interatomic exchange interactions, the *spin-wave stiffness* D can be calculated. Due to possible oscillations in the exchange interactions as a function of the distance, it becomes necessary to introduce a damping parameter η to assure convergence of the summation. D can then be obtained by evaluating the limit $\eta \to 0$ of

$$D = \frac{2}{3} \sum_{ij} \frac{J_{ij}}{\sqrt{M_i M_j}} r_{ij}^2 \exp\left(-\eta \frac{r_{ij}}{a_{\text{lat}}}\right), \tag{4}$$

as described in [47]. Here, M_i and M_j are the local magnetic moments at sites i and j, J_{ij} is the exchange coupling between the magnetic moments at sites i and j, and r_{ij} is the distance between the atoms i and j. This formalism can be extended to a multisublattice system [48].

Chemical disorder might affect the spin-wave stiffness of the system. In order to take this into account, 200 supercells were constructed using the atomistic spin dynamics package UPPASD [49]. The supercells consisting of $16\times16\times16$ unit cells were constructed in such a way as to represent the studied concentrations. (For more details see Appendix A.) Equation (4) was then evaluated in each supercell, yielding the spin-wave stiffness for 200 different configurations. The results were averaged and the standard deviation was calculated.

Finally, with the spin-wave stiffness determined as described above, the *exchange stiffness* A can be calculated from [50]

$$A = \frac{D M_S(T)}{2 g \mu_B}. \tag{5}$$

Here, g is the Landé g-factor of the electron, μ_B the Bohr magneton, and $M_S(T)$ the magnetization density of the system for a given temperature T, which for $T = 0$ K corresponds to the saturation magnetization.

From the first-principles calculations, the magnetic properties for ordered NiMnSb and chemically disordered $Ni_{1-x}Mn_{1+x}Sb$ were studied. To obtain the values of the exchange stiffness A for $T = 300$ K, the exchange interactions from the *ab initio* calculations were used in conjunction with the value of the magnetization at $T = 300$ K obtained from Monte Carlo simulations.

III. RESULTS

A. Magnetization

The values of $\mu_0 M_{\text{eff}}$ are plotted in Fig. 2(a) as red dots. The effective magnetization is considerably lower than the saturation magnetization $\mu_0 M_S$, which was independently assessed using superconducting quantum interference device (SQUID) measurements and alternating gradient magnetometry (AGM). The values for $\mu_0 M_S$ correspond to a saturation magnetization between 3.5 μ_B/unit formula and 3.9 μ_B/u.f., with the latter value being within the error bars of the theoretically expected value of 4.0 μ_B/u.f. for stoichiometric NiMnSb [51]. A reduction of M_S is expected in Mn-rich NiMnSb alloys due to the antiferromagnetic coupling of the Mn_{Ni} defects to the Mn lattice in the $C1_b$ structure of the half-Heusler

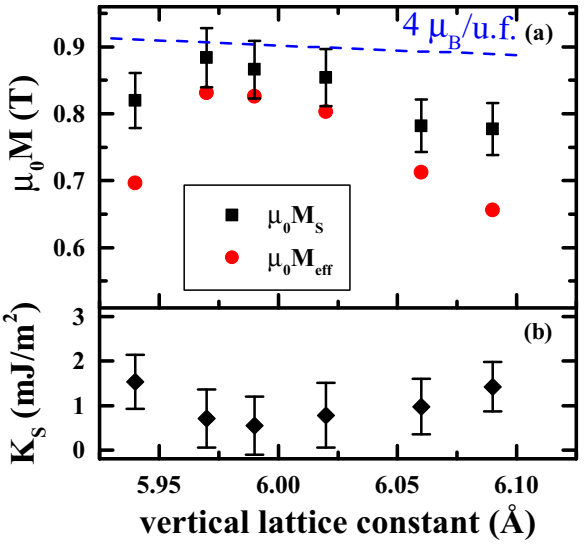

FIG. 2. (Color online) (a) M_S and M_{eff} as functions of vertical lattice constant. The theoretical value of 4.0 μ_B/u.f. is shown by the blue dashed line. (b) The calculated surface anisotropy density follows from the difference between M_S and M_{eff}.

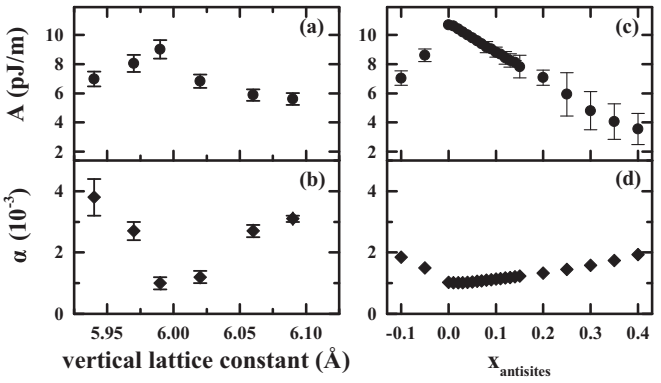

FIG. 3. (a, b) The exchange stiffness and Gilbert damping constant, respectively, obtained from FMR measurements, plotted as a function of the vertical lattice constant. (c, d) The corresponding values obtained from first-principles calculations for $T = 300$ K. Negative values for x imply the introduction of Ni_{Mn} antisites and positive values are related to Mn_{Ni} antisite defects. The error bars in (c) are the standard deviations from repeated first-principles calculations with 200 randomized supercells.

material [29]. An even stronger reduction is observed for the Ni-rich sample 1, which is in accordance with the formation of Ni_{Mn} antisites [52].

While the measurement error for M_S is comparatively large due to uncertainties in the volume determination, the error bars for M_{eff}, as obtained from ferromagnetic resonance, are negligible. NiMnSb films have been shown to possess a small but substantial perpendicular magnetic anisotropy, which can arise from either interfacial anisotropy or lattice strain [10,12]. To quantify the difference observed between M_S and M_{eff}, we assume a uniaxial perpendicular anisotropy due to a surface anisotropy energy density K_S, which is known to follow the relation [53]

$$\mu_0 M_{\text{eff}} = \mu_0 M_S - \frac{2K_S}{M_S d}. \tag{6}$$

The K_S calculated in this way has values between 0.5 and 1.5 mJ/m^2, as shown in Fig. 2(b); these are comparable to the surface anisotropies obtained in other crystalline thin-film systems [54]. Although the film thicknesses in our set vary unsystematically, we can observe systematic behavior of K_S with the vertical lattice constant, with an apparent minimum under the conditions where stoichiometric NiMnSb is expected—that is, for samples 2 and 3. The increasing values for off-stoichiometric NiMnSb can be thus attributed to the concomitant increase in lattice defects, and thus of surface defects, in these films.

B. Exchange stiffness and Gilbert damping

The experimentally determined exchange stiffness, as a function of the vertical lattice constant, and the Gilbert damping parameter are shown in Figs. 3(a) and 3(b), respectively. The minimum damping observed in our measurements is 1.0×10^{-3} for sample 3, and so is within stoichiometric composition. Sample 1, with a deficiency of Mn atoms, showed nonlinear linewidth behavior at low frequencies, which vanished for out-of-plane measurements (not shown). This is typical with the presence of two-magnon scattering processes [54]. However, the damping is considerably lower in all samples than in a permalloy film of comparable thickness.

The exchange stiffness and Gilbert damping obtained from the first-principles calculations are shown in Figs. 3(c) and 3(d), respectively. For both parameters, the experimental trends are reproduced quantitatively, with A having a maximum and α a minimum value at stoichiometry.

As the concentration of both Mn or Ni antisites increases, the exchange stiffness decreases. This behavior can be explained by analyzing the terms in the expression for the spin-wave stiffness, Eq. (4). It turns out that the new exchange couplings J_{ij}, which appear when antisites are present, play a major role, whereas changes in the atomic magnetic moments or the saturation magnetization appear to be relatively unimportant. Mn antisites in the Ni sublattice (i.e., excess Mn) have a strong (2 mRy) antiferromagnetic coupling to the Mn atoms in the adjacent Mn layers. This results in a negative contribution to D compared to the stoichiometric case, where this interaction is not present. On the other hand, Ni antisites in the Mn sublattice have a negative in-plane exchange coupling of 0.3 mRy to their nearest-neighbor Mn atoms, with a frustrated antiferromagnetic coupling to the Ni atoms in the adjacent Ni plane. The net effect is a decreasing spin-wave stiffness as the composition moves away from stoichiometry. The calculated values of A are around 30% larger than the experimental results, which is the same degree of overestimation we recently observed in a study of doped permalloy films [55]. It thus seems to be inherent in our calculations from first principles.

The calculated Gilbert damping also agrees well with the experimental values. The damping has its minimum value of 1.0×10^{-3} at stoichiometry and increases with a surplus of Ni faster than with the same surplus of Mn. Both Mn and Ni antisites will act as impurities and it is thus

reasonable to attribute the observed increase in damping at off-stoichiometry to impurity scattering. While the damping at stoichiometry also agrees quantitatively, the increase in damping is underestimated in the calculations compared to the experimental values.

Despite the fact that the calculations here focus purely on the formation of Mn_{Ni} or Ni_{Mn} antisites, they are nonetheless capable of reproducing the experimental trends well. However, interstitials—that is, Mn or Ni surplus atoms in the vacant sublattice—may also be a possible off-stoichiometric defect in our system [52]. We have calculated their effects and can therefore discuss about the existence of interstitials in our samples. A large fraction of Mn interstitials seems unlikely, as an increase in the saturation magnetization can be predicted through calculations, contrary to the experimental trend; see Fig. 2(a). On the other hand, the existence of Ni interstitials may be compatible with the observed experimental trend, as they decrease the saturation magnetization—albeit at a slower rate than Ni antisites and slower than experimentally observed. Judging from the measured data, it is therefore likely that excess Ni exists in the samples as both antisites and interstitials.

IV. CONCLUSIONS

In summary, we have found that off-stoichiometry in the epitaxially grown half-Heusler alloy NiMnSb has a significant impact on the material's magnetodynamic properties. In particular, the exchange stiffness can be altered by a factor of about 2 while keeping the Gilbert damping very low (≈5 times lower than in permalloy films). This is a unique combination of properties and opens up for the use of NiMnSb in, e.g., magnonic circuits, where a small spin-wave damping is desired. At the stoichiometric composition, the saturation magnetization and exchange stiffness take on their maximum values, whereas the Gilbert damping parameter is at its minimum. These experimentally observed results are reproduced by calculations from first principles. Using these calculations, we can also explain the microscopic mechanisms behind the observed trends. We also conclude that interstitial Mn is unlikely to be present in the samples. The observed effects can be used to fine tune the magnetic properties of NiMnSb films towards their specific requirements in spintronic devices.

ACKNOWLEDGMENTS

We acknowledge financial support from the Göran Gustafsson Foundation, the Swedish Research Council (VR), Energimyndigheten (STEM), the Knut and Alice Wallenberg Foundation (KAW), the Carl Tryggers Foundation (CTS), and the Swedish Foundation for Strategic Research (SSF). F.G. acknowledges financial support from the University of Würzburg's "Equal Opportunities for Women in Research and Teaching" program. This work was also supported initially by the European Commission FP7, Contract ICT-257159 "MACALO." A.B. acknowledges eSSENCE. The computer simulations were performed on resources provided by the Swedish National Infrastructure for Computing (SNIC) at the National Supercomputer Centre (NSC) and High Performance Computing Center North (HPC2N).

APPENDIX: TREATMENT OF DISORDER IN THE SIMULATIONS

The treatment of random alloy systems requires methods that consider both the effects of the disorder at the first-principles level and in the atomistic spin dynamics simulations (ASD). The disorder can be taken into account by two main approaches: the use of supercells and the coherent potential approximation (CPA) [40,41].

In the supercell approach, the atoms are distributed either randomly or using special quasirandom structures (SQS) [56] with the corresponding concentration of atomic species. Increasing the supercell size results in an improved description of the alloy decomposition. However, in practice, due to the use of limited supercell sizes, an ensemble averaging needs to be performed over several specific realizations of the disorder configuration. On the other hand, CPA yields average properties over an infinite number of disorder configurations at the expense of using a single-site approximation and neglecting any short-range order possibly present in the system.

In this work, we have therefore employed the CPA description of disorder for the *electronic structure* calculations, mimicking the disorder by replacing the real system with an effective medium using scattering formalisms and Green's functions. When treating the disorder effects in the *atomistic spin dynamics*, however, we use the supercell approach together with the average exchange couplings between atoms, as obtained from CPA. The spin-wave stiffness for a particular disorder configuration is thus calculated by randomly distributing atoms over a large supercell. This consists of $16\times16\times16$ minimal possible unit cells with one atom on each Ni and Mn site according to the composition of the alloy. Atoms on the Sb sublattice were not taken into account due to their very low magnetic moment, and therefore the ASD simulations were evaluated in supercells with 8192 magnetic atoms. Then, to obtain an effective spin-wave stiffness, an average over 200 of these disorder configuration realizations is done. Furthermore, calculating the standard deviation of the observable yields an estimation of the statistical error in our method.

[1] R. Okura, Y. Sakuraba, T. Seki, K. Izumi, M. Mizuguchi, and K. Takanashi, High-power rf oscillation induced in half-metallic Co_2MnSi layer by spin-transfer torque, Appl. Phys. Lett. **99**, 052510 (2011).

[2] T. Yamamoto, T. Seki, T. Kubota, H. Yako, and K. Takanashi, Zero-field spin torque oscillation in Co_2(Fe, Mn)Si with a point contact geometry, Appl. Phys. Lett. **106**, 092406 (2015).

[3] P. Dürrenfeld, F. Gerhard, M. Ranjbar, C. Gould, L. W. Molenkamp, and J. Åkerman, Spin Hall effect-controlled magnetization dynamics in NiMnSb, J. Appl. Phys. **117**, 17E103 (2015).

[4] R. A. de Groot, F. M. Mueller, P. G. van Engen, and K. H. J. Buschow, New Class of Materials: Half-Metallic Ferromagnets, Phys. Rev. Lett. **50**, 2024 (1983).

[5] D. Ristoiu, J. P. Nozières, C. N. Borca, T. Komesu, H. k. Jeong, and P. A. Dowben, The surface composition and spin polarization of NiMnSb epitaxial thin films, Europhys. Lett. **49**, 624 (2000).

[6] T. Kubota, S. Tsunegi, M. Oogane, S. Mizukami, T. Miyazaki, H. Naganuma, and Y. Ando, Half-metallicity and Gilbert damping constant in $Co_2Fe_xMn_{1-x}Si$ Heusler alloys depending on the film composition, Appl. Phys. Lett. **94**, 122504 (2009).

[7] G. M. Müller, J. Walowski, M. Djordjevic, G.-X. Miao, A. Gupta, A. V. Ramos, K. Gehrke, V. Moshnyaga, K. Samwer, J. Schmalhorst, A. Thomas, A. Hütten, G. Reiss, J. S. Moodera, and M. Münzenberg, Spin polarization in half-metals probed by femtosecond spin excitation, Nat. Mater. **8**, 56 (2009).

[8] M. Jourdan, J. Minàr, J. Braun, A. Kronenberg, S. Chadov, B. Balke, A. Gloskovskii, M. Kolbe, H. J. Elmers, G. Schönhense, H. Ebert, C. Felser, and M. Kläui, Direct observation of half-metallicity in the Heusler compound Co_2MnSi, Nat. Commun. **5**, 3974 (2014).

[9] B. Heinrich, G. Woltersdorf, R. Urban, O. Mosendz, G. Schmidt, P. Bach, L. Molenkamp, and E. Rozenberg, Magnetic properties of NiMnSb(001) films grown on InGaAs/InP(001), J. Appl. Phys. **95**, 7462 (2004).

[10] A. Koveshnikov, G. Woltersdorf, J. Q. Liu, B. Kardasz, O. Mosendz, B. Heinrich, K. L. Kavanagh, P. Bach, A. S. Bader, C. Schumacher, C. Rüster, C. Gould, G. Schmidt, L. W. Molenkamp, and C. Kumpf, Structural and magnetic properties of NiMnSb/InGaAs/InP(001), J. Appl. Phys. **97**, 073906 (2005).

[11] S. Trudel, O. Gaier, J. Hamrle, and B. Hillebrands, Magnetic anisotropy, exchange and damping in cobalt-based full-Heusler compounds: An experimental review, J. Phys. D: Appl. Phys. **43**, 193001 (2010).

[12] A. Riegler, Ph.D. thesis, Universität Würzburg (2011).

[13] P. Bach, A. S. Bader, C. Rüster, C. Gould, C. R. Becker, G. Schmidt, L. W. Molenkamp, W. Weigand, C. Kumpf, E. Umbach, R. Urban, G. Woltersdorf, and B. Heinrich, Molecular-beam epitaxy of the half-Heusler alloy NiMnSb on (In,Ga)As/InP (001), Appl. Phys. Lett. **83**, 521 (2003).

[14] P. Bach, C. Rüster, C. Gould, C. R. Becker, G. Schmidt, and L. W. Molenkamp, Growth of the half-Heusler alloy NiMnSb on (In,Ga)As/InP by molecular beam epitaxy, J. Cryst. Growth **251**, 323 (2003).

[15] F. Gerhard, C. Schumacher, C. Gould, and L. W. Molenkamp, Control of the magnetic in-plane anisotropy in off-stoichiometric NiMnSb, J. Appl. Phys. **115**, 094505 (2014).

[16] M. Tsoi, A. G. M. Jansen, J. Bass, W.-C. Chiang, M. Seck, V. Tsoi, and P. Wyder, Excitation of a Magnetic Multilayer by an Electric Current, Phys. Rev. Lett. **80**, 4281 (1998).

[17] J. Slonczewski, Excitation of spin waves by an electric current, J. Magn. Magn. Mater. **195**, 261 (1999).

[18] T. J. Silva and W. H. Rippard, Developments in nano-oscillators based upon spin-transfer point-contact devices, J. Magn. Magn. Mater. **320**, 1260 (2008).

[19] M. Madami, S. Bonetti, G. Consolo, S. Tacchi, G. Carlotti, G. Gubbiotti, F. B. Mancoff, M. A. Yar, and J. Åkerman, Direct observation of a propagating spin wave induced by spin-transfer torque, Nat. Nanotechnol. **6**, 635 (2011).

[20] S. Bonetti, V. Tiberkevich, G. Consolo, G. Finocchio, P. Muduli, F. Mancoff, A. Slavin, and J. Åkerman, Experimental Evidence of Self-Localized and Propagating Spin Wave Modes in Obliquely Magnetized Current-Driven Nanocontacts, Phys. Rev. Lett. **105**, 217204 (2010).

[21] R. K. Dumas, E. Iacocca, S. Bonetti, S. R. Sani, S. M. Mohseni, A. Eklund, J. Persson, O. Heinonen, and J. Åkerman, Spin-Wave-Mode Coexistence on the Nanoscale: A Consequence of the Oersted-Field-Induced Asymmetric Energy Landscape, Phys. Rev. Lett. **110**, 257202 (2013).

[22] R. K. Dumas, S. R. Sani, S. M. Mohseni, E. Iacocca, Y. Pogoryelov, P. K. Muduli, S. Chung, P. Dürrenfeld, and J. Åkerman, Recent advances in nanocontact spin-torque oscillators, IEEE Trans. Magn. **50**, 4100107 (2014).

[23] V. E. Demidov, S. Urazhdin, H. Ulrichs, V. Tiberkevich, A. Slavin, D. Baither, G. Schmitz, and S. O. Demokritov, Magnetic nano-oscillator driven by pure spin current, Nat. Mater. **11**, 1028 (2012).

[24] R. H. Liu, W. L. Lim, and S. Urazhdin, Spectral Characteristics of the Microwave Emission by the Spin Hall Nano-Oscillator, Phys. Rev. Lett. **110**, 147601 (2013).

[25] V. E. Demidov, H. Ulrichs, S. V. Gurevich, S. O. Demokritov, V. S. Tiberkevich, A. N. Slavin, A. Zholud, and S. Urazhdin, Synchronization of spin Hall nano-oscillators to external microwave signals, Nat. Commun. **5**, 3179 (2014).

[26] Z. Duan, A. Smith, L. Yang, B. Youngblood, J. Lindner, V. E. Demidov, S. O. Demokritov, and I. N. Krivorotov, Nanowire spin torque oscillator driven by spin orbit torques, Nat. Commun. **5**, 5616 (2014).

[27] M. Ranjbar, P. Dürrenfeld, M. Haidar, E. Iacocca, M. Balinskiy, T. Q. Le, M. Fazlali, A. Houshang, A. A. Awad, R. K. Dumas, and J. Åkerman, CoFeB-based spin Hall nano-oscillators, IEEE Magn. Lett. **5**, 3000504 (2014).

[28] C. Kumpf, A. Stahl, I. Gierz, C. Schumacher, S. Mahapatra, F. Lochner, K. Brunner, G. Schmidt, L. W. Molenkamp, and E. Umbach, Structure and relaxation effects in thin semiconducting films and quantum dots, Phys. Status Solidi C **4**, 3150 (2007).

[29] M. Ekholm, P. Larsson, B. Alling, U. Helmersson, and I. A. Abrikosov, Ab initio calculations and synthesis of the off-stoichiometric half-Heusler phase $Ni_{1-x}Mn_{1+x}Sb$, J. Appl. Phys. **108**, 093712 (2010).

[30] A. M. Portis, Low-lying spin wave modes in ferromagnetic films, Appl. Phys. Lett. **2**, 69 (1963).

[31] B. Lenk, G. Eilers, J. Hamrle, and M. Münzenberg, Spin-wave population in nickel after femtosecond laser pulse excitation, Phys. Rev. B **82**, 134443 (2010).

[32] I. S. Maksymov and M. Kostylev, Broadband stripline ferromagnetic resonance spectroscopy of ferromagnetic films, multilayers and nanostructures, Physica E **69**, 253 (2015).

[33] Georg Woltersdorf, Ph.D. thesis, Simon Fraser University (2004).

[34] N. Mecking, Y. S. Gui, and C.-M. Hu, Microwave photovoltage and photoresistance effects in ferromagnetic microstrips, Phys. Rev. B **76**, 224430 (2007).

[35] A. Conca, E. Th. Papaioannou, S. Klingler, J. Greser, T. Sebastian, B. Leven, J. Lösch, and B. Hillebrands, Annealing influence on the Gilbert damping parameter and the exchange constant of CoFeB thin films, Appl. Phys. Lett. **104**, 182407 (2014).

[36] M. van Kampen, C. Jozsa, J. T. Kohlhepp, P. LeClair, L. Lagae, W. J. M. de Jonge, and B. Koopmans, All-Optical Probe of Coherent Spin Waves, Phys. Rev. Lett. **88**, 227201 (2002).

[37] S. S. Kalarickal, P. Krivosik, M. Wu, C. E. Patton, M. L. Schneider, P. Kabos, T. J. Silva, and J. P. Nibarger, Ferromagnetic resonance linewidth in metallic thin films: Comparison of measurement methods, J. Appl. Phys. **99**, 093909 (2006).

[38] Kh. Zakeri, J. Lindner, I. Barsukov, R. Meckenstock, M. Farle, U. von Hörsten, H. Wende, W. Keune, J. Rocker, S. S. Kalarickal, K. Lenz, W. Kuch, K. Baberschke, and Z. Frait, Spin dynamics in ferromagnets: Gilbert damping and two-magnon scattering, Phys. Rev. B **76**, 104416 (2007).

[39] H. Ebert, D. Ködderitzsch, and J. Minár, Calculating condensed matter properties using the KKR-Green's function method, Recent developments and applications, Rep. Prog. Phys. **74**, 096501 (2011).

[40] P. Soven, Coherent-potential model of substitutional disordered alloys, Phys. Rev. **156**, 809 (1967).

[41] G. M. Stocks, W. M. Temmerman, and B. L. Gyorffy, Complete Solution of the Korringa-Kohn-Rostoker Coherent-Potential-Approximation Equations: Cu-Ni Alloys, Phys. Rev. Lett. **41**, 339 (1978).

[42] I. Garate and A. MacDonald, Gilbert damping in conducting ferromagnets, II. Model tests of the torque-correlation formula, Phys. Rev. B **79**, 064404 (2009).

[43] S. Mankovsky, D. Ködderitzsch, G. Woltersdorf, and H. Ebert, First-principles calculation of the Gilbert damping parameter via the linear response formalism with application to magnetic transition metals and alloys, Phys. Rev. B **87**, 014430 (2013).

[44] H. Ebert, S. Mankovsky, K. Chadova, S. Polesya, J. Minár, and D. Ködderitzsch, Calculating linear-response functions for finite temperatures on the basis of the alloy analogy model, Phys. Rev. B **91**, 165132 (2015).

[45] A. I. Liechtenstein, M. I. Katsnelson, and V. A. Gubanov, Exchange interactions and spin-wave stiffness in ferromagnetic metals, J. Phys. F **14**, L125 (1984).

[46] A. I. Liechtenstein, M. I. Katsnelson, V. P. Antropov, and V. A. Gubanov, Local spin density functional approach to the theory of exchange interactions in ferromagnetic metals and alloys, J. Magn. Magn. Mater. **67**, 65 (1987).

[47] M. Pajda, J. Kudrnovský, I. Turek, V. Drchal, and P. Bruno, *Ab initio* calculations of exchange interactions, spin-wave stiffness constants, and Curie temperatures of Fe, Co, and Ni, Phys. Rev. B **64**, 174402 (2001).

[48] J. Thoene, S. Chadov, G. Fecher, C. Felser, and J. Kübler, Exchange energies, Curie temperatures and magnons in Heusler compounds, J. Phys. D: Appl. Phys. **42**, 084013 (2009).

[49] B. Skubic, J. Hellsvik, L. Nordström, and O. Eriksson, A method for atomistic spin dynamics simulations: Implementation and examples, J. Phys.: Condens. Matter **20**, 315203 (2008).

[50] C. A. F. Vaz, J. A. C. Bland, and G. Lauhoff, Magnetism in ultrathin film structures, Rep. Prog. Phys. **71**, 056501 (2008).

[51] T. Graf, C. Felser, and S. S. P. Parkin, Simple rules for the understanding of Heusler compounds, Prog. Solid State Chem. **39**, 1 (2011).

[52] B. Alling, S. Shallcross, and I. A. Abrikosov, Role of stoichiometric and nonstoichiometric defects on the magnetic properties of the half-metallic ferromagnet NiMnSb, Phys. Rev. B **73**, 064418 (2006).

[53] Y.-C. Chen, D.-S. Hung, Y.-D. Yao, S.-F. Lee, H.-P. Ji, and C. Yu, Ferromagnetic resonance study of thickness-dependent magnetization precession in Ni_{80} Fe_{20} films, J. Appl. Phys. **101**, 09C104 (2007).

[54] X. Liu, W. Zhang, M. J. Carter, and G. Xiao, Ferromagnetic resonance and damping properties of CoFeB thin films as free layers in MgO-based magnetic tunnel junctions, J. Appl. Phys. **110**, 033910 (2011).

[55] Y. Yin, F. Pan, M. Ahlberg, M. Ranjbar, P. Dürrenfeld, A. Houshang, M. Haidar, L. Bergqvist, Y. Zhai, R. K. Dumas, A. Delin, and J. Åkerman, Tunable permalloy-based films for magnonic devices, Phys. Rev. B **92**, 024427 (2015).

[56] A. Zunger, S.-H. Wei, L. G. Ferreira, and J. E. Bernard, Special Quasirandom Structures, Phys. Rev. Lett. **65**, 353 (1990).